Supporting Information

High Dynamic Range Nanowire Resonators

Juan Molina[1], Javier E. Escobar[1], Daniel Ramos[1], Eduardo Gil-Santos[1], José J. Ruz[1], Javier Tamayo[1], Álvaro San Paulo[1], Montserrat Calleja[1]*

[1]Instituto de Micro y Nanotecnología, IMN-CNM, CSIC (CEI UAM+CSIC)

Isaac Newton 8, 28760, Tres Cantos, Madrid. Spain

*Corresponding author's e-mail address: alvaro.sanpaulo@csic.es;

Contents

1. Theoretical analysis of dynamic range in flexural beam resonators

1.1. Nonlinear equation of motion and frequency response

A general approach to derive the nonlinear equation of motion of a bending beam with a large aspect ratio (much larger length L than transversal dimensions), regardless of its clamp configuration, is based on Hamilton's principle and Galerkin's method.[30,31] The Lagrangian $\mathcal{L}$ of the system is defined in terms of its kinetic energy E_K and potential energy U as:

$$\mathcal{L} = E_K(u) - U(u) \tag{S1}$$

where $u = u(\xi, t)$ is the displacement of the beam along its bending direction X, written as a function of the normalized position along the beam ($\xi = Z/L$) and time t. If we consider an approximate unimodal solution given by

$$u(\xi, t) = \phi(\xi)x(t) \tag{S2}$$

where $\phi(\xi)$ is the mode shape of the associated linear problem and $x(t)$ is an unknow function of time (we normalize $\phi(\xi)$ such that $x(t)$ represents the actual displacement of the beam at the maximum deflection point), then our problem is reduced to solving the temporal Euler-Lagrange equation:

$$\frac{\partial \mathcal{L}}{\partial x} - \frac{d}{dt}\left(\frac{\partial \mathcal{L}}{\partial \dot{x}}\right) = 0 \tag{S3}$$

In sections 1.1.1 and 1.1.2, we follow this approach considering the first nonlinear terms that appear in the Lagrangian of singly clamped (SC) and doubly clamped (DC) beams, respectively, in order to obtain their equations of motion; and in section 1.1.3, we derive an equivalent nonlinear frequency response for both cases after solving these equations.

1.1.1. Equation of motion for singly clamped beams

In a singly clamped beam, nonlinear terms appearing both in its potential energy (geometric terms) and kinetic energy (inertial terms) are equally significant.[24] The former occur because the bending curvature has an intrinsic nonlinear dependence on the displacement u, which starts to manifest when u is large enough. On the other hand, inertial terms appear as a consequence of the inextensibility condition, which considers that the neutral axis of the beam has a constant length. Including the first nonlinear terms derived from these considerations, the kinetic and potential energy of the beam read:[30]

$$E_K = \frac{\rho LS}{2}\int_0^1 \left[\dot{u}^2 + \frac{1}{4L^2}\left(\frac{d}{dt}\int_0^{\xi} u'^2(\zeta)d\zeta\right)^2\right] d\xi \tag{S4a}$$

$$U = \frac{EI}{2L^3}\int_0^1 \left[(u'')^2 + \frac{1}{L^2}(u'u'')^2\right] d\xi \tag{S4b}$$

where an apostrophe denotes derivative with respect to ξ, a dot refers to time derivative; and homogeneous density (ρ), Young's modulus (E), cross section area (S) and second moment of area with respect to Y axis (I) have been considered. The first terms appearing on the right-hand side of equations (S4) are the linear contributions from which the harmonic oscillator equation would be derived, whereas the second terms are the first nonlinear corrections (lowest order in u'/L). If we combine equations (S1)-(S4), we obtain the equation of motion of a singly clamped nonlinear beam resonator:

$$m\ddot{x} + \frac{m\omega_0}{Q}\dot{x} + kx + \frac{\beta_G}{L^2}x^3 + \frac{\beta_I}{L^2}(x\dot{x}^2 + x^2\ddot{x}) = F_0\cos(\omega t) \tag{S5}$$

where an external force with amplitude F_0 and frequency ω has been added, as well as a phenomenological damping term associated to a finite quality factor Q; and the effective mass (m), effective spring constant (k), natural frequency (ω_0), geometrical nonlinear coefficient (β_G), and inertial nonlinear coefficient (β_I) are given by:

$$m = \rho LS\int_0^1 \phi(\xi)^2 d\xi \tag{S6a}$$

$$k = \frac{EI}{L^3}\int_0^1 \phi''(\xi)^2 d\xi \tag{S6b}$$

$$\omega_0^2 = \frac{k}{m} \tag{S6c}$$

$$\beta_G = \frac{2EI}{L^3}\int_0^1 [\phi'(\xi)\phi''(\xi)]^2 d\xi \tag{S6d}$$

$$\beta_I = \rho LS\int_0^1 \left[\int_0^{\xi}\phi'(\zeta)^2 d\zeta\right]^2 d\xi \tag{S6e}$$

As mentioned in section 1.1, $\phi(\xi)$ is the mode shape of the associated linear problem:[31]

$$\phi(\xi) = \frac{1}{2}\left\{\cosh(k_0\xi) - \cos(k_0\xi) + \frac{\cos(k_0) + \cosh(k_0)}{\sin(k_0) + \sinh(k_0)}[\sin(k_0\xi) - \sinh(k_0\xi)\,]\right\} \tag{S7}$$

where $k_0 = 1.875$, since we are only considering in the first flexural mode, and the $1/2$ factor results from the normalization criterion $\phi(1) = 1$.

1.1.2. Equation of motion for doubly clamped beams

The dominant nonlinear mechanism in doubly clamped beams is bending-induced tension, arising from the fact that when a doubly clamped beam deflects, it necessarily stretches.[19] The clamps at both ends may also introduce a residual tension resulting from an extension or compression of the beam in equilibrium with respect to its rest length, but we do not consider such residual tension in our calculations. Thus, for the doubly clamped configuration, the kinetic and potential energy can be expressed as:

$$E_K = \frac{\rho LS}{2}\int_0^1 \dot{u}^2 d\xi \tag{S8a}$$

$$U = \frac{EI}{2L^3}\int_0^1 (u'')^2 d\xi + \frac{ES}{8L^3}\left[\int_0^1 (u')^2 d\xi\right]^2 \tag{S8b}$$

The second term on the right-hand side of the potential energy accounts for the geometric nonlinearity arising from bending-induced tension in doubly clamped beams, and it dominates over other nonlinear terms comparable to those calculated for singly clamped beams in the previous section. With an analogous procedure to the one followed there, we can combine (S1)-(S3) with (S8) to obtain the Duffing-type equation of motion of a doubly clamped nonlinear beam resonator:

$$m\ddot{x} + \frac{m\omega_0}{Q}\dot{x} + kx + \frac{\beta_{DC}}{L^2}x^3 = F_0\cos(\omega t) \tag{S9}$$

where the dominating geometric nonlinear coefficient for this configuration (β_{DC}) is defined as:

$$\beta_{DC} = \frac{ES}{2L}\left[\int_0^1 \phi'(\xi)^2 d\xi\right]^2 \tag{S10}$$

and every other common magnitude is defined analogously to the singly clamped case, but considering the corresponding mode shape of a doubly clamped beam:

$$\phi(\xi) = 0.6297\left\{\cosh(k_0\xi) - \cos(k_0\xi) + \frac{\cos(k_0) - \cosh(k_0)}{\sin(k_0) - \sinh(k_0)}\left[\sin(k_0\xi) - \sinh(k_0\xi)\right]\right\} \tag{S11}$$

with $k_0 = 4.730$, and normalized to satisfy $\phi(1/2) = 1$.

1.1.3. Nonlinear frequency response

The frequency response derived from equations of motion (S5) and (S9) can be similarly obtained by considering an approximate solution with the form:

$$x = a_1 \cos(\omega t) + a_2 \sin(\omega t) = a \cos(\omega t - \Phi) \tag{S12}$$

where the amplitude (a) and the phase shift (Φ) of the response are defined by

$$a^2 = a_1^2 + a_2^2 \tag{S13a}$$

$$\tan \Phi = \frac{a_2}{a_1} \tag{S13b}$$

Introducing these expressions into equations (S5) and (S9), we obtain an equivalent approximate frequency response for both configurations:

$$a^2(\omega) = \frac{a_0^2}{\left[Q\left(\frac{\omega^2}{\omega_0^2} - 1\right) - \frac{3Q\alpha_{NL}}{4L^2} a^2(\omega)\right]^2 + \frac{\omega^2}{\omega_0^2}} \tag{S14}$$

where we have designated $a_0 = QF_0/k$, and the difference between singly clamped and doubly clamped nonlinear response is included into a global nonlinear coefficient α_{NL}. For the case of singly clamped beams, this coefficient is defined by

$$\alpha_{NL}(SC) = \frac{\beta_G}{k} - \frac{2}{3}\frac{\beta_I}{m} \tag{S15}$$

and it can be regarded as a result of the balance between geometrical (α_G) and inertial (α_I) contributions:

$$\alpha_{NL}(SC) = \alpha_G - \alpha_I \tag{S16a}$$

$$\alpha_G = \frac{2\int_0^1 [\phi'(\xi)\phi''(\xi)]^2 d\xi}{\int_0^1 \phi''(\xi)^2 d\xi} \tag{S16b}$$

$$\alpha_I = \frac{2}{3}\frac{\int_0^1 \left[\int_0^\xi \phi'(\zeta)^2 d\zeta\right]^2 d\xi}{\int_0^1 \phi(\xi)^2 d\xi} \tag{S16c}$$

According to equation (S14), when α_{NL} is positive, a sufficiently large driving force deforms the Lorentzian resonance response curve of the linear case so that the peak amplitude occurs at a resonance frequency $\omega_R > \omega_0$ (stiffening). Oppositely, when α_{NL} is negative then the resonance frequency shifts to $\omega_R < \omega_0$ (softening). For the first flexural mode of a singly clamped beam with homogeneous cross-section, α_G is slightly larger than α_I and the global nonlinear coefficient obtained after computing (S16) for the mode shape in (S7) is $\alpha_{NL} = 0.0517$, thus producing a stiffening effect. Because of this delicate balance, the opposite behavior has been observed on cantilevers with length over width ratios lower than 10,[24] but our model is not considering such short aspect ratio regime.

On the other hand, for the case of doubly clamped beams, α_{NL} is given by

$$\alpha_{NL}(DC) = \frac{\beta_{DC}}{k} = \frac{SL^2}{2I} \frac{\left[\int_0^1 \phi'(\xi)^2 d\xi\right]^2}{\int_0^1 \phi''(\xi)^2 d\xi} \tag{S17}$$

which is a positive coefficient, always resulting in a stiffening effect at large amplitude. Contrary to what we found for the SC case, the nonlinear coefficient in DC beams is not only a numerical factor, but it depends on the geometry of the beam. The common numerical factor resulting from the integrals appearing in (S17) can be computed for the mode shape in (S11) to obtain

$$\alpha_{NL}(DC) = 0.0600 \frac{SL^2}{I} \tag{S18}$$

This expression already shows that because of the different nature of the dominating nonlinear mechanism in a doubly clamped beam, its nonlinear coefficient is proportional to the square of its aspect ratio L/D (having into account that $S/I \propto D^{-2}$), which results into the appearance of nonlinear effects at much lower amplitudes for this clamping configuration when typical aspect ratios are considered. Table S1 in section 1.3 shows the expressions of α_{NL} for the different beam geometries treated in this work.

1.2. Onset of nonlinearity

The common frequency response described by (S14) allows to characterize the transition from linear to nonlinear regime as well as to define magnitudes that represent such transition. Here we describe three relevant magnitudes that represent three different thresholds of the linear to nonlinear transition: the multivalued resonance threshold amplitude, the critical amplitude and the 1 dB compression point.

1.2.1. Multivalued resonance threshold

If we consider the case $\alpha_{NL} > 0$ (stiffening response), as we have seen that is expected for the first flexural mode of both singly clamped and doubly clamped beams, equation (S14) can be rewritten as follows:

$$a^2(\omega) = \frac{a_0^2}{\left[Q\left(\frac{\omega^2}{\omega_0^2} - 1\right) - \frac{a^2(\omega)}{a_M^2}\right]^2 + \frac{\omega^2}{\omega_0^2}} \tag{S19}$$

where the multivalued resonance threshold amplitude (a_M) has been defined as

$$a_M = \frac{2L}{\sqrt{3Q\alpha_{NL}}} \tag{S20}$$

This magnitude has several remarkable peculiarities. First, if we evaluate (S19) at the natural frequency ω_0, which approximately corresponds to the resonance frequency of the linear case ($\alpha_{NL} = 0$) when $Q \gg 1$, we obtain

$$a_0 = a(\omega_0)\sqrt{1 + \left[\frac{a(\omega_0)}{a_M}\right]^4} \tag{S21}$$

and two different regimes can be defined from this expression. For the case $a(\omega_0) \ll a_M$, we recover the response of the linear oscillator such that the amplitude is proportional to the applied force:

$$a(\omega_0) \approx a_0 \tag{S22}$$

On the other hand, when $a(\omega_0) \gg a_M$, the amplitude turns to be proportional to the cubic root of the applied force:

$$a(\omega_0) \approx a_M^{2/3} a_0^{1/3} \tag{S23}$$

This gives the first significant meaning to a_M: it can be regarded as a characteristic amplitude that defines the transition from linear to nonlinear regime. Moreover, if we compare the purely linear response in (S22) with the purely nonlinear response in (S23), we find that the cutting point of these curves (straight lines if we plot them in log-log scale) occurs exactly at $a(\omega_0) = a_M$, as shown in Figure 1c of the main text. Another property of this parameter can be found by introducing this last equality into equation (S21) to obtain $a_0/a_M = \sqrt{2}$, which means that a_M is the amplitude of the resonator (evaluated at ω_0) when the nonlinearity reduces the expected response for a purely linear case by a factor of $\sqrt{2}$.

Finally, the property to which the multivalued resonance threshold amplitude a_M owes its name can be derived by searching for the onset of bifurcation when we evaluate the response given by (S19) at the resonance frequency (ω_R), which for $Q \gg 1$ reads:

$$\omega_R^2 \approx \omega_0^2\left(1+\frac{a_0^2}{Qa_M^2}\right) \tag{S24}$$

For the resonance to start to be multivalued, the implicit cubic equation in a^2 associated to (S19) must have three real roots: one simple root (a_I) with zero slope, which corresponds to the maximum amplitude of the spectrum (resonance); and one double root (a_{II}), which corresponds to a lower amplitude value with an infinite slope. If we compute these roots considering (S24) and $Q \gg 1$, we obtain $a_I = \sqrt{2}a_M$ and $a_{II} = a_M$. Thus, since the amplitude at resonance is approximately equal to a_0, we find that the onset of bifurcation at such amplitude occurs exactly for the curve satisfying $a(\omega_0) = a_M$ that we discussed above.

An equivalent analysis can be performed if we consider the case $\alpha_{NL} < 0$, for which a plus sign must replace the minus sign preceding the nonlinear term in equation (S19), and the same conclusions about the parameter a_M would result from such analysis, with the only difference that the resonance would show a softening behavior at large amplitudes (the plus sign in (S24) should be replaced by a minus sign).

1.2.2. Critical amplitude

The critical amplitude (a_c) is another relevant magnitude of a nonlinear oscillator, both from a physical and a mathematical point of view. It is defined as the amplitude for which the response of the resonator starts to show a bifurcation at some frequency. This is equivalent to the case in which the implicit cubic equation in a^2 associated to (S19) has a triple root. If we calculate this triple root and consider $Q \gg 1$, we obtain the following expression for the critical amplitude:

$$a_c \approx \frac{2\sqrt{2}}{3^{3/4}}\frac{L}{\sqrt{Q|\alpha_{NL}|}} \tag{S25}$$

occurring at a frequency ω_c that is neither the natural frequency nor the resonance frequency:

$$\omega_c \approx \omega_0\left(1+\frac{\sqrt{3}}{2Q}\right) \tag{S26}$$

with the plus sign replaced by a minus sign in the case $\alpha_{NL} < 0$. If we compare (S20) and (S25), we can relate the parameter a_M with the critical amplitude:

$$a_M = \sqrt{\frac{\sqrt{3}}{2}}a_c \approx 0.931a_c \tag{S27}$$

It is important to note that although a_c is larger than a_M, the driving force required to reach the critical amplitude (onset of bifurcation at some frequency) is lower than the driving force required to reach the curve for which $a(\omega_0) = a_M$ (onset of bifurcation at resonance frequency), and thus the critical amplitude represents a more restrictive reference for the upper limit of the linear regime.

1.2.3. 1 dB Compression point

We finally describe the magnitude that is used to define the onset of nonlinearity regarding practical applications. The parameters introduced in the last two sections, a_M and a_c, are associated to bifurcations and infinite slopes in the frequency response curves that are not desirable by typical experimental procedures designed to work within the linear operation regime. For this reason, a more restrictive parameter to delimit the linear regime is commonly used: the 1 dB compression point, referred to as the point where the oscillation amplitude at the natural frequency $a_{1dB}(\omega_0)$ is 1 dB lower than the amplitude that would result from a purely linear response for the same driving force, a_0. If we apply this definition to equation (S21), we obtain the following expression for the 1 dB compression point:

$$a_{1dB}(\omega_0) = \left(10^{1/10}-1\right)^{1/4}a_M \simeq 0.713a_M \tag{S28}$$

This is the parameter that we have used to define the upper limit of the dynamic range and, combining expressions (S27) and (S28), it can be related to the critical amplitude by

$$a_{1dB}(\omega_0) = \left(10^{1/10}-1\right)^{1/4}\sqrt{\frac{\sqrt{3}}{2}}a_c \simeq 0.664a_c \tag{S29}$$

If we now evaluate this same 1 dB compression curve at the resonance frequency ω_R, we obtain a value $a_{1dB}(\omega_R)$ which, for $Q \gg 1$, is equal to the amplitude that would be expected for the linear case evaluated at ω_0, that is, 1 dB larger than $a_{1dB}(\omega_0)$:

$$a_{1dB}(\omega_R) = 10^{1/20}\left(10^{1/10} - 1\right)^{1/4} a_M \simeq 0.800 a_M \tag{S30}$$

resulting into the more extended relation found in previous works:[19,34]

$$a_{1dB}(\omega_R) \simeq 0.745 a_c \tag{S31}$$

It is important to note that $a_{1dB}(\omega_R)$ is not the amplitude of the spectrum that shows a 1 dB compression at resonance (for $Q \gg 1$, the response evaluated at resonance that follows the backbone curve defined by (S24) does not show any compression), but it is the amplitude at resonance of the spectrum that shows a 1 dB compression at the fixed natural frequency. Since this definition is less straightforward than the definition of $a_{1dB}(\omega_0)$, and having into account that the lower limit of the dynamic range is also evaluated at the natural frequency, we have considered more convenient to use relations (S28) and (S29) for the analysis developed in this work. However, our results can be easily compared to those reported in previous works and our model can be adapted to the definitions given by (S30) and (S31) just by having into account that slight 1 dB difference.

1.3. Expressions for dynamic range

As described in the main text, we consider thermomechanical noise as the dominant noise source of the amplitude signal, and we define the intrinsic dynamic ratio r_D as the ratio of the amplitude at the onset of nonlinearity (1 dB compression point) to the lowest measurable amplitude (thermomechanical spectral density integrated for the measurement bandwidth Δf):

$$r_D = \frac{a_{1dB}(\omega_0)}{\sqrt{2S_x^{\mathrm{Th}}\Delta f}} \simeq 0.291\sqrt{\frac{L^2 m\omega_0^3}{k_B T Q^2 \Delta f |\alpha_{NL}|}} \tag{S32}$$

This relation, given in terms of m, ω_0 and α_{NL}, can be applied both to singly clamped and doubly clamped beams with different geometries. Table S1 includes the expressions of such parameters for rectangular, hexagonal and circular cross section geometries, considering a uniform cross section, as well as the resulting 1 dB compression amplitude obtained from (S28). Slight variations are found when comparing distinct geometries for a given clamping configuration, whereas more significant differences appear between SC and

DC beams. The most remarkable one is that, because of the different nonlinear mechanisms that dominate the appearance of nonlinearities in SC and DC beams (see section 1.1), the 1 dB compression amplitude is geometry-dependent and proportional to the transversal characteristic magnitude D in DC beams, whereas it has a unique value proportional to the length L in SC beams.

Clamp	Geometry	S	I	m	ω_0	α_{NL}	a_{1dB}
SC	Rectangular	$W \cdot D$	$\frac{WD^3}{12}$	$0.250\rho LWD$	$1.015\sqrt{\frac{E}{\rho}\frac{D}{L^2}}$	0.0517	$3.623\frac{L}{\sqrt{Q}}$
	Hexagonal	$\frac{3\sqrt{3}D^2}{8}$	$\frac{5\sqrt{3}D^4}{256}$	$0.162\rho LD^2$	$0.802\sqrt{\frac{E}{\rho}\frac{D}{L^2}}$	0.0517	$3.623\frac{L}{\sqrt{Q}}$
	Circular	$\frac{\pi D^2}{4}$	$\frac{\pi D^4}{64}$	$0.196\rho LD^2$	$0.879\sqrt{\frac{E}{\rho}\frac{D}{L^2}}$	0.0517	$3.623\frac{L}{\sqrt{Q}}$
DC	Rectangular	$W \cdot D$	$\frac{WD^3}{12}$	$0.397\rho LWD$	$6.459\sqrt{\frac{E}{\rho}\frac{D}{L^2}}$	$0.719\left(\frac{L}{D}\right)^2$	$0.971\frac{D}{\sqrt{Q}}$
	Hexagonal	$\frac{3\sqrt{3}D^2}{8}$	$\frac{5\sqrt{3}D^4}{256}$	$0.258\rho LD^2$	$5.106\sqrt{\frac{E}{\rho}\frac{D}{L^2}}$	$1.151\left(\frac{L}{D}\right)^2$	$0.768\frac{D}{\sqrt{Q}}$
	Circular	$\frac{\pi D^2}{4}$	$\frac{\pi D^4}{64}$	$0.311\rho LD^2$	$5.593\sqrt{\frac{E}{\rho}\frac{D}{L^2}}$	$0.959\left(\frac{L}{D}\right)^2$	$0.841\frac{D}{\sqrt{Q}}$

Table S1. Cross section, second moment of area, effective mass, natural frequency, nonlinear coefficient and 1dB compression amplitude for different geometries of SC and DC beams with uniform cross section. In rectangular cross section beams, D refers to thickness and W to width.

Table S2 shows the dynamic ratio of SC and DC beams with uniform cross section calculated by means of equation (S32), according to the parameters from table S1. Regarding the differences between both clamping configurations in terms of order of magnitude, we can extract an approximate relation valid for every geometry considered in this work:

$$\frac{r_D(SC)}{r_D(DC)} \approx 0.2\frac{L}{D} \tag{S33}$$

which predicts a larger dynamic range for singly clamped beams if we consider the aspect ratio of typical devices. The particular expressions for each geometry are listed in table S2.

Geometry	r_D (Singly Clamped)	r_D (Doubly Clamped)	$r_D(SC)/r_D(DC)$
Rectangular	$0.655 \cdot \sqrt{WD}\left(\frac{D}{L}\right)^{3/2}\sqrt{\frac{E^{3/2}}{Q^2 k_B T \Delta f \sqrt{\rho}}}$	$3.549 \cdot \sqrt{WD}\left(\frac{D}{L}\right)^{5/2}\sqrt{\frac{E^{3/2}}{Q^2 k_B T \Delta f \sqrt{\rho}}}$	$0.185\frac{L}{D}$
Hexagonal	$0.371 \cdot D\left(\frac{D}{L}\right)^{3/2}\sqrt{\frac{E^{3/2}}{Q^2 k_B T \Delta f \sqrt{\rho}}}$	$1.589 \cdot D\left(\frac{D}{L}\right)^{5/2}\sqrt{\frac{E^{3/2}}{Q^2 k_B T \Delta f \sqrt{\rho}}}$	$0.233\frac{L}{D}$
Circular	$0.468 \cdot D\left(\frac{D}{L}\right)^{3/2}\sqrt{\frac{E^{3/2}}{Q^2 k_B T \Delta f \sqrt{\rho}}}$	$2.195 \cdot D\left(\frac{D}{L}\right)^{5/2}\sqrt{\frac{E^{3/2}}{Q^2 k_B T \Delta f \sqrt{\rho}}}$	$0.213\frac{L}{D}$

Table S2. Dynamic ratio of singly and doubly clamped beams with uniform cross section and different geometries.

1.4. Fundamental mass detection limits

Having an analytical expression for the dynamic range of a beam allows to predict its mass resolution limit (δm), under the assumptions described in the main text, according to:[47]

$$\delta m = \frac{m}{Qr_D} \tag{S34}$$

Combining this equation with tables S1 and S2 provides the expressions shown in table S3, from which an approximate relation valid for every geometry can be extracted to describe the differences between both clamping configurations in terms of order of magnitude:

$$\frac{\delta m(DC)}{\delta m(SC)} \approx 0.3\frac{L}{D} \tag{S35}$$

which predicts a lower mass resolution limit for singly clamped beams if we consider the aspect ratio of typical devices. The particular expressions for each geometry are listed in table S3.

Geometry	δm (Singly Clamped)	δm (Doubly Clamped)	$\delta m(DC)/\delta m(SC)$
Rectangular	$0.382 \cdot \sqrt{WD^3}\left(\frac{L}{D}\right)^{5/2}\sqrt{\frac{k_B T \Delta f \rho^{5/2}}{E^{3/2}}}$	$0.112 \cdot \sqrt{WD^3}\left(\frac{L}{D}\right)^{7/2}\sqrt{\frac{k_B T \Delta f \rho^{5/2}}{E^{3/2}}}$	$0.293\frac{L}{D}$
Hexagonal	$0.438 \cdot D^2\left(\frac{L}{D}\right)^{5/2}\sqrt{\frac{k_B T \Delta f \rho^{5/2}}{E^{3/2}}}$	$0.162 \cdot D^2\left(\frac{L}{D}\right)^{7/2}\sqrt{\frac{k_B T \Delta f \rho^{5/2}}{E^{3/2}}}$	$0.370\frac{L}{D}$
Circular	$0.420 \cdot D^2\left(\frac{L}{D}\right)^{5/2}\sqrt{\frac{k_B T \Delta f \rho^{5/2}}{E^{3/2}}}$	$0.142 \cdot D^2\left(\frac{L}{D}\right)^{7/2}\sqrt{\frac{k_B T \Delta f \rho^{5/2}}{E^{3/2}}}$	$0.338\frac{L}{D}$

Table S3. Mass resolution limit of singly and doubly clamped beams with uniform cross section and different geometries.

1.5. Including tapering effect in singly clamped beams

The expressions obtained so far regarding singly clamped beams with a circular or hexagonal uniform cross section can be generalized to consider a linearly decreasing diameter from base (D_0) to tip (D_{tip}), which is a characteristic feature of bottom-up grown nanowires. If we introduce a tapering coefficient $\alpha_T = 1 - D_{tip}/D_0$, the diameter of the beam can be expressed as a function of the position along its normalized length:

$$D(\xi) = D_0(1 - \alpha_T \xi) \tag{S36}$$

Considering this relation, the kinetic and potential energies in (S4) must be rewritten as

$$E_K = \frac{\rho L S_0}{2}\int_0^1 (1 - \alpha_T \xi)^2 \left[\dot{u}^2 + \frac{1}{4L^2}\left(\frac{d}{dt}\int_0^{\xi} u'^2(\zeta) d\zeta\right)^2\right] d\xi \tag{S37a}$$

$$U = \frac{EI_0}{2L^5}\int_0^1 (1 - \alpha_T \xi)^4 [(Lu'')^2 + (u'u'')^2] d\xi \tag{S37b}$$

where the section and the second moment of area at the base of the beam have been introduced (S_0 and I_0, respectively). If we apply the analysis described in section 1.1 to these expressions, we arrive to the same equation of motion found in (S5) after redefining the coefficients from (S6) as follows:

$$m = \rho L S_0 \int_0^1 (1 - \alpha_T \xi)^2 \phi(\xi)^2 d\xi \tag{S38a}$$

$$k = \frac{EI_0}{L^3}\int_0^1 (1 - \alpha_T \xi)^4 \phi''(\xi)^2 d\xi \tag{S38b}$$

$$\omega_0^2 = \frac{k}{m} \tag{S38c}$$

$$\beta_G = \frac{2EI_0}{L^3}\int_0^1 (1-\alpha_T\xi)^4[\phi'(\xi)\phi''(\xi)]^2 d\xi \tag{S38d}$$

$$\beta_I = \rho L S_0 \int_0^1 (1-\alpha_T\xi)^2 \left[\int_0^{\xi} \phi'(\zeta)^2 d\zeta\right]^2 d\xi \tag{S38e}$$

where the mode shape of the associated linear problem $\phi(\xi)$ is not represented by (S7) anymore, but it must also consider the tapered geometry. The mode shape and the natural frequencies of tapered beams have already been numerically computed in a previous work,[28] and here we extend the analysis to describe the relation of other relevant parameters with the tapering coefficient, obtaining the results shown in table S4. Since α_T only takes values within the interval [0,1], every function of α_T that we have defined can be approximated by a polynomial fitting after numerically solving the corresponding integrals for a discrete set of values within that interval, as shown in Figure S1.

Table S5 includes the expressions for the dynamic ratio of tapered singly clamped beams with hexagonal and circular cross section, showing that the dynamic range of a very tapered beam ($\alpha_T = 0.9$) is 8.2 dB lower than the dynamic range of a uniform beam (note that this difference only depends on the function $h(\alpha_T)$ and is therefore independent of the cross-section geometry).

Finally, if we consider a singly clamped beam with tapered geometry according to the general expression of mass resolution limit provided in table S4, we obtain the relations included in table S6, showing that the mass resolution limit is around one order of magnitude lower for a very tapered beam ($\alpha_T = 0.9$) than for a uniform beam (note that this difference only depends on the function $j(\alpha_T)$ and is therefore independent of the cross section geometry).

Natural frequency	Expression	$\omega_0 = \left[\frac{k_0(\alpha_T)}{L}\right]^2 \sqrt{\frac{EI_0}{\rho S_0}}$
	Function	$k_0(\alpha_T) = \sqrt[4]{\frac{\int_0^1 (1-\alpha_T\xi)^4 \phi''(\xi)^2 d\xi}{\int_0^1 (1-\alpha_T\xi)^2 \phi(\xi)^2 d\xi}}$
	Fitting	$k_0(\alpha_T) \approx 1.875 + 0.336\alpha_T + 0.697\alpha_T^2 - 1.115\alpha_T^3 + 1.150\alpha_T^4$
Effective mass	Expression	$m = g(\alpha_T)\rho L S_0$
	Function	$g(\alpha_T) = \int_0^1 (1-\alpha_T\xi)^2 \phi(\xi)^2 d\xi$
	Fitting	$g(\alpha_T) \approx 0.250 - 0.448\alpha_T + 0.203\alpha_T^2$
Nonlinear onset	Expression	$a_{1dB}(\omega_0) = (10^{1/10} - 1)^{1/4} \frac{2L}{\sqrt{3Q\alpha_{NL}(\alpha_T)}}$
	Function	$\alpha_{NL}(\alpha_T) = \frac{2\int_0^1 (1-\alpha_T\xi)^4 [\phi'(\xi)\phi''(\xi)]^2 d\xi}{\int_0^1 (1-\alpha_T\xi)^4 \phi''(\xi)^2 d\xi} - \frac{2}{3}\frac{\int_0^1 (1-\alpha_T\xi)^2 \left[\int_0^\xi \phi'(\zeta)^2 d\zeta\right]^2 d\xi}{\int_0^1 (1-\alpha_T\xi)^2 \phi(\xi)^2 d\xi}$
	Fitting	$\alpha_{NL}(\alpha) \approx 0.0517 + 0.0651\alpha_T - 0.188\alpha_T^2 + 0.548\alpha_T^3 - 0.364\alpha_T^4$
Dynamic ratio	Expression	$r_D = 4.222 \cdot h(\alpha_T) \sqrt{\frac{(EI_0)^{3/2}}{L^3 k_B T Q^2 \Delta f \sqrt{\rho S_0}}}$
	Function	$h(\alpha_T) = \frac{1}{\sqrt{\frac{g(0)k_0^6(0)}{\lvert\alpha_{NL}(0)\rvert}}} \sqrt{\frac{g(\alpha_T)k_0^6(\alpha_T)}{\lvert\alpha_{NL}(\alpha_T)\rvert}}$
	Fitting	$h(\alpha_T) \approx 1 - 0.677\alpha_T$
Mass resolution limit	Expression	$\delta m = 0.0592 \cdot j(\alpha_T) \sqrt{\frac{k_B T \Delta f L^5 (\rho S_0)^{5/2}}{(EI_0)^{3/2}}}$
	Function	$j(\alpha_T) = \frac{1}{\sqrt{\frac{g(0)\lvert\alpha_{NL}(0)\rvert}{k_0^6(0)}}} \sqrt{\frac{g(\alpha_T)\lvert\alpha_{NL}(\alpha_T)\rvert}{k_0^6(\alpha_T)}}$
	Fitting	$j(\alpha_T) \approx 1 - 1.171\alpha_T + 0.200\alpha_T^2$

Table S4. Functions of the tapering coefficient appearing in some relevant expressions treated in this work and approximate polynomial fittings of such functions obtained from numerical analysis. The intercepts of the fittings are fixed at the values found for the uniform cross section case.

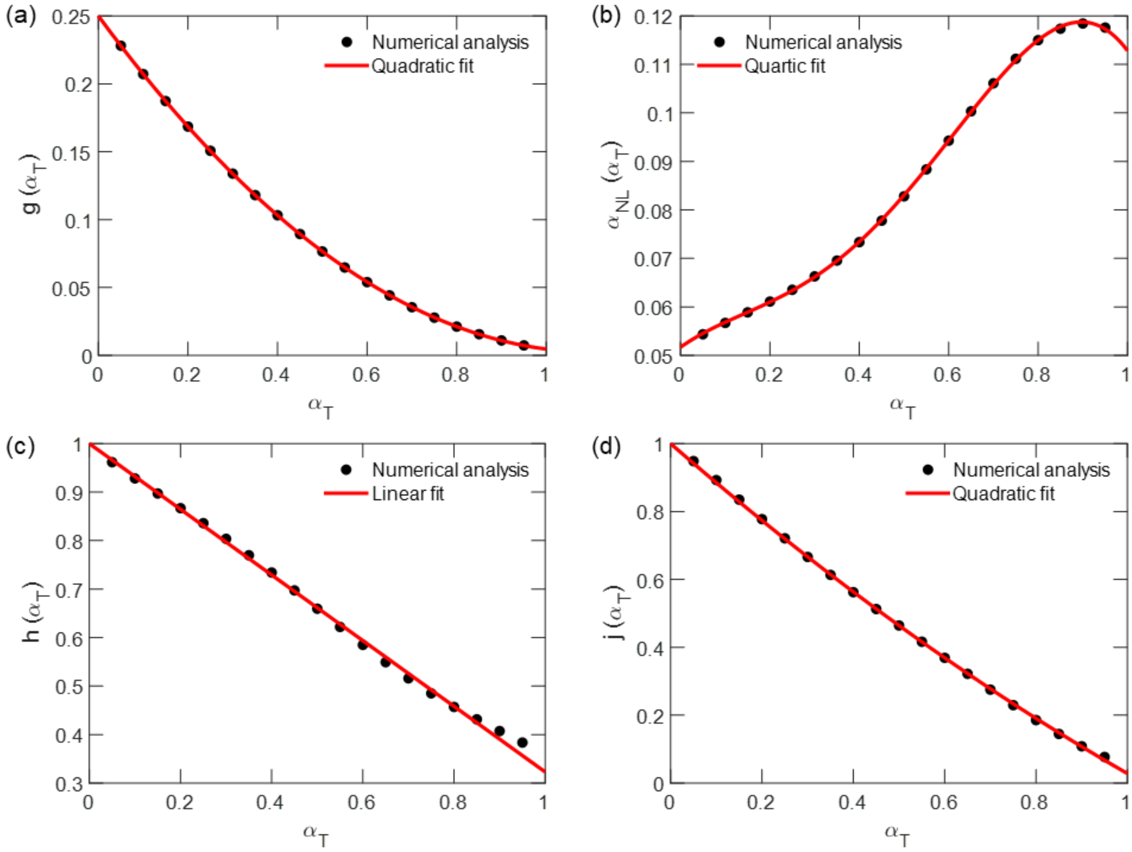

Figure S1. Functions of the tapering coefficient. Numerical calculations for a set of 19 α_T values and polynomial fittings of the functions g **(a)**, α_{NL} **(b)**, h **(c)**, and j **(d)**. The expressions defining these functions and the corresponding fittings are shown in table 3. The fitting of the function k_0 can be found in a previous work.[28]

Geometry	r_D (Singly Clamped, Tapered)	$DR\ (\alpha_T = 0.9) - DR\ (\alpha_T = 0)$
Hexagonal	$0.371 \cdot h(\alpha_T) \cdot D_0 \left(\frac{D_0}{L}\right)^{3/2} \sqrt{\frac{E^{3/2}}{Q^2 k_B T \Delta f \sqrt{\rho}}}$	$-8.2\ dB$
Circular	$0.468 \cdot h(\alpha_T) \cdot D_0 \left(\frac{D_0}{L}\right)^{3/2} \sqrt{\frac{E^{3/2}}{Q^2 k_B T \Delta f \sqrt{\rho}}}$	$-8.2\ dB$

Table S5. Dynamic ratio of tapered singly clamped beams with hexagonal and circular cross section.

Geometry	δm (Singly Clamped, Tapered)	$\delta m\ (\alpha_T = 0.9)/\delta m\ (\alpha_T = 0)$
Hexagonal	$0.438 \cdot j(\alpha_T) \cdot\ D_0^2 \left(\frac{L}{D_0}\right)^{5/2} \sqrt{\frac{k_B T \Delta f \rho^{5/2}}{E^{3/2}}}$	0.108
Circular	$0.420 \cdot j(\alpha_T) \cdot\ D_0^2 \left(\frac{L}{D_0}\right)^{5/2} \sqrt{\frac{k_B T \Delta f \rho^{5/2}}{E^{3/2}}}$	0.108

Table S6. Mass resolution limit of tapered singly clamped beams with hexagonal and circular cross section.

2. Si Nanowire growth and characterization

Si nanowires (NW) were grown in a Nanoinnova "CVDCube" atmospheric pressure chemical vapor deposition (AP-CVD) system by the vapor liquid solid (VLS) mechanism with $SiCl_4$ vapor as precursor. We used colloidal Au nanoparticles (NP) as catalyst with three different nominal diameter values: 100, 150 and 250 nm (Sigma-Aldrich). Au NPs were deposited on Si (111) substrates without any predetermined pattern and without any sort of prefabricated micro or nanostructure. Before NP deposition, substrates were thoroughly treated in ultrasounds by sequential immersions in acetone, isopropyl alcohol and DI water. A 10s immersion in HF (5%) was performed in order to remove native oxide. 60s immersion in Poly-L-lysine was also performed in order to improve Au NP adhesion. NP deposition was completed by immersion of the treated substrates in the colloidal Au NP suspension with 1:20 reduced concentration with respect to original values. The NWs were grown at 825 °C directing the liquid $SiCl_4$ precursor into the tubular quartz reactor by flowing 30 sccm of inert Ar gas through a bubbler kept at 0 °C. H_2 (10% in Argon) was introduced with a flow of 120 sccm. In order to vary the nanowire length, four growth times were used: 10, 15, 22.5 and 34 min. After the growth time, the reactive gases were purged with Ar from the tube for another 5 min. Very similar average growth rates around 1.1 μm/min where observed regardless of the catalyst NP diameter. Table S7 specifies the Au catalyst NP diameter and growth time used for each of the Si NWs under analysis in this work.

Au NP D [nm]	Growth time [min]	Si NW #	Si NW L [μm]	Si NW D_0 [nm]	Si NW L/D_0	Si NW α_T
150	34	**2**	44.2	256	173	0.88
150	34	**3**	43.7	276	158	0.81
150	34	**1**	43.2	241	179	0.89
250	22.5	**9**	27.1	326	83	0.46
250	22.5	**8**	27.0	294	92	0.52
150	22.5	**4**	25.9	199	130	0.72
150	22.5	**6**	25.7	237	108	0.69
150	22.5	**7**	25.1	219	115	0.73
250	15	**16**	19.5	422	46	0.24
250	15	**12**	19.3	347	56	0.27
250	15	**11**	18.1	309	58	0.28
150	15	**5**	17.6	212	83	0.34
150	15	**10**	17.5	190	92	0.38
250	10	**15**	11.6	338	34	0.17
250	10	**20**	11.0	326	34	0.18
150	10	**17**	10.8	183	59	0.31
150	10	**18**	10.7	194	55	0.24
150	10	**19**	10.5	203	52	0.29
150	10	**14**	10.3	192	53	0.29
100	10	**13**	10.3	145	71	0.46

Table S7. Au catalyst NP diameter and growth time used for each of the Si NWs under analysis in this work.

3. Transduction of Si nanowire vibration

3.1 Experimental set-up details

The experimental set-up (Figure 2c in the main text) uses a fiber-coupled diode laser (TopMode-633, Toptica Photonics AG, λ=633 nm). Output power and polarization are manually controlled with a variable attenuator and birefringence loops, respectively. The values of incident optical power used range from 72 μW to 216 μW, depending on the sample, high enough to resolve the thermomechanical signal of nanowires at practical acquisition times ($\tau \lesssim$ 1s) but without inducing any observable optomechanical back-action effect. On the other hand, the polarization is aligned with the longitudinal axis of the nanowires in order to maximize the backscattered intensity, optimizing transduction sensitivity.[8] After this fiber stage, a triplet lens collimator provides a nearly Gaussian free-space beam, with its optical axis (Y axis) oriented perpendicular to the longitudinal axis of the nanowires (Z axis).

The beam is focused on the Si NWs grown near the edges of the substrate (Figure 2a) using a 20× objective with 0.42 numerical aperture, which results into a laser spot waist diameter ($2w_0$) of around 4 μm. A nanopositioning stage controls the relative X-Z position of the sample with respect to the probe beam incidence point as well as its focus. A piezoelectric actuator below the sample allows the excitation of flexural modes.

The backscattered beam is collected by an unsegmented Si photoreceiver coupled to a low-noise transimpedance amplifier. The resulting electrical signal is then processed either by a digital acquisition (DAQ) board or by a lock-in amplifier (LIA). The LIA reference signal is delivered to the piezoelectric actuator in the case of driven vibrations. The DAQ board is synchronized both with a signal generator, which can also be connected to the actuator, and with the nanopositioning stage, allowing the acquisition of the signal of the photoreceiver as the relative sample–laser beam position is scanned. All the measurements are performed in high vacuum ($\sim 10^{-5}$ mbar) and at substrate temperatures of around 325 K (a stationary heating effect is induced by the nanopositioner stage). A CCD camera with white light illumination coupled to the system by a pellicle beamsplitter provides top-view optical images in order to navigate the sample surface and locate nanowires of interest. A flip mount adapter allows to remove the pellicle beamsplitter from the beam path during measurements in order to reduce optical losses.

3.2 Transduction sensitivity

The transduction mechanism underlying the readout of mechanical resonances used in this work is based on the modulation of backscattered light induced by nanowire vibrations. Besides the use of an unsegmented photodetector, similar methods have already been used in previous works.[9,15] An example corresponding to nanowire #18 of the mean optical power P collected by the unsegmented photodetector (DC component) as a function of the X-Z position with respect to the incident laser beam is shown in Figure S2a. When the beam is focused on the nanowire, the optical gradient lies in the X-Z plane, enabling the transduction of X-Z displacements. However, in this configuration, the flexural doublet modes of the nanowire occur in the X-Y plane,[10] and thus only the projection along the X axis of each doublet component can be detected. Since these components are orthogonal, at least one of them shows a significant projection along the X axis. Given that the resonance frequencies of the components of a doublet are very close (although nondegenerate in high vacuum due to slight geometric asymmetries in nanowire cross section), we have focused our study on the component presenting a better alignment with the X axis (higher signal).

The sensitivity (σ) of the transduction mechanism relates the power spectral density (PSD) of nanowire vibrations in m^2/Hz units (S_X) with the PSD of the measured power signal in W^2/Hz units (S_P) through $S_P = \sigma^2 S_X + S_{BG}$, where an uncorrelated background noise (S_{BG}) has been added. The transduction mechanism implies that the sensitivity is proportional to the absolute value of the optical power gradient $\partial P/\partial X$ along the X direction, so that $\sigma \propto \partial P/\partial X$.[10] Figure S2c shows the corresponding X-Z mapping of the collected power gradient along the X direction for the same nanowire as in Figure S2a. $\partial P/\partial X$ depends on the Z position because the coupling of Mie modes depends on the diameter of the nanowire,[1,9] which varies along its length due to its tapered geometry, thus resulting into the varying backscattering efficiency along Z as already seen in Figure S2a. As a consequence, the highest signal is not necessarily obtained at the maximum displacement Z position (tip of the NW), as would be expected for a homogeneous cross section NW. In longer and more tapered nanowires, several Mie modes can be coupled along their length.

Figures S2b and S2d show a cross-section along the X direction in the maps from Figures S2a and S2c, respectively, revealing two relevant remarks regarding the transduction mechanism. First, within the area of interaction between the nanowire and the laser beam, which is comparable to the diameter of the later ($2w_0$), the collected power gradient profile shows two symmetric local maxima at an approximate nanowire-laser beam relative position $X = \pm X_M$, with $X_M \approx w_0/2$. In order to maximize transduction sensitivity, our measurements were taken at either of these local maxima. The second remark is that the collected power profile is approximately linear (i.e., nearly constant transduction sensitivity) along a ~1 μm span centered at the measuring positions $\pm X_M$. This provides a wide transduction linearity that has enabled the experiments performed in this work. In section 3.3, we analyze such linearity in more detail.

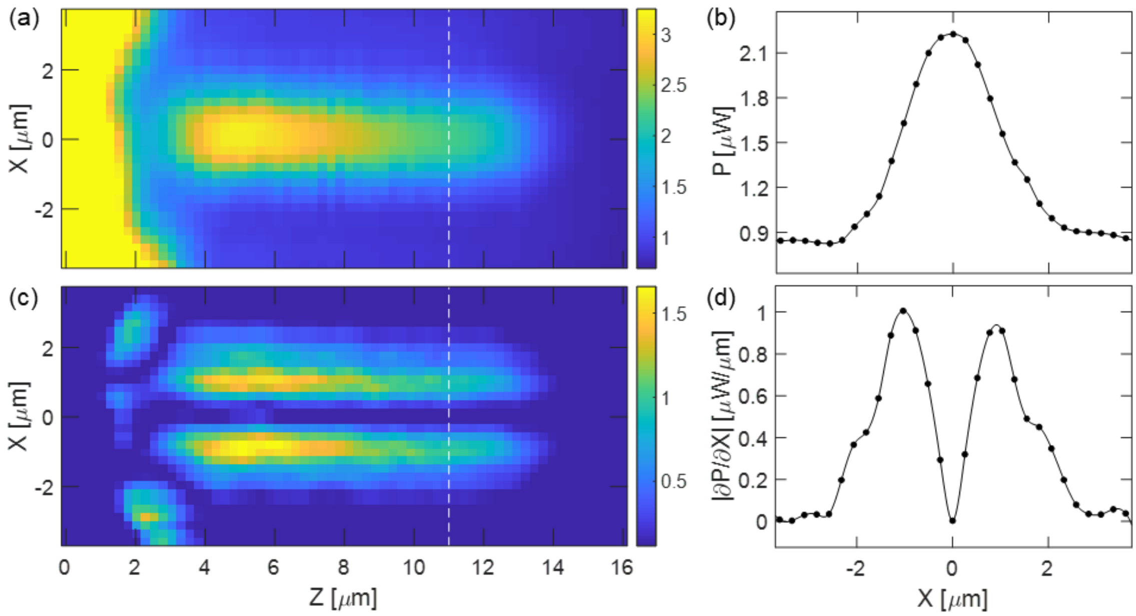

Figure S2. Backscattering modulation transduction mechanism. (a) Mapping of collected optical power, *P*, as a function of the relative nanowire−laser beam position, measured for NW #18 (the longitudinal axis of the nanowire is located along *X*=0, and the saturated yellow region corresponds to the reflection from the substrate). **(b)** Profile along the white dashed line of the previous map (*Z*=11 μm) showing the variation of backscattered power as the laser beam is translated along the *X* direction. **(c)** Gradient along *X* (absolute value) of the collected optical power shown in (a). **(d)** Profile along the white dashed line of the previous map (*Z*=11 μm) showing the variation of backscattered power *X*-gradient as the laser beam is translated along the *X* direction.

Remarkably, the sensitivity also depends on a diverse number of factors as nanowire diameter, relative *X-Z* probe position, optical power, amplifier gain, and angle between the actual vibration direction and *X* axis. Thus, a single calibration constant valid for every nanowire and measurement condition cannot be obtained from the measurement of $|\partial P/\partial X|_{X_M}$. Alternatively, since we know the effective mass of our nanowires from SEM characterization and our transduction method is able to resolve thermal fluctuations for the whole set of nanowires studied, the thermomechanical calibration method provides a more practical approach to determine the nanowire vibration amplitude in length units.[37] Figure S3 provides the calibrated spectrum of nanowire #18 measured at an input power of 144 μW (same nanowire considered in Figure S2). The fitting to a thermally driven linear oscillator response provides a transduction sensitivity of 0.50 W/m and a noise floor of 4.62 pm/√Hz, which represents an estimation of the minimum detectable displacement for this concrete example.

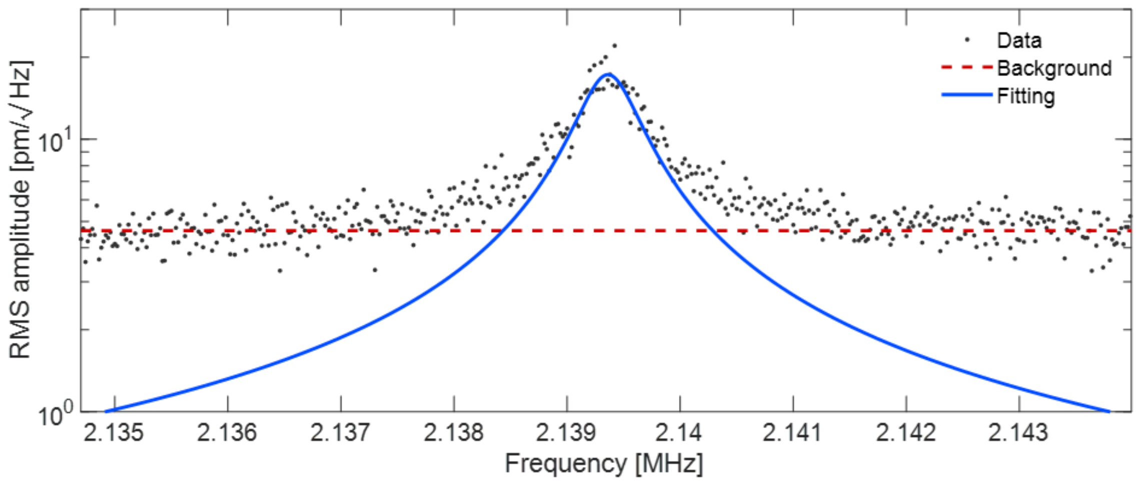

Figure S3. Thermomechanical calibration of vibration signal. Calibrated thermomechanical noise spectrum of NW #18, measured with the DAQ board at an equivalent resolution bandwidth of 10 Hz, fitted to a thermally driven linear oscillator response (equation equivalent to (S14) for the case $\alpha_{NL} = 0$) with an added white background noise (in the plot, the background has been subtracted from the fitting).

3.3. Linear range

As described in the previous section, the transduction sensitivity depends critically on the optical power gradient $\partial P/\partial X$ along the X direction, so that the variation of $|\partial P/\partial X|_{\mathrm{X_M}}$ as a function of the projection of the vibration amplitude of the nanowire along this direction determines the linear range of the transduction. An estimation of the transduction linear range for the example treated in section 3.2 can be obtained from the collected power profile shown in Figure S2b. Since it is related to the intensity profile of the laser spot, an approximated analytical expression of the collected power profile can be obtained from a Gaussian fitting of the (X, P) measured points:

$$P(X) = Ae^{-\frac{X^2}{2B^2}} + C \tag{S39}$$

where A, B and C are positive fitting parameters, and the Gaussian curve has been centered at $X = 0$ (as well as the measured points). The derivative of this curve can be written as:

$$P'(X) = -\frac{AX}{B^2}e^{-\frac{X^2}{2B^2}} \tag{S40}$$

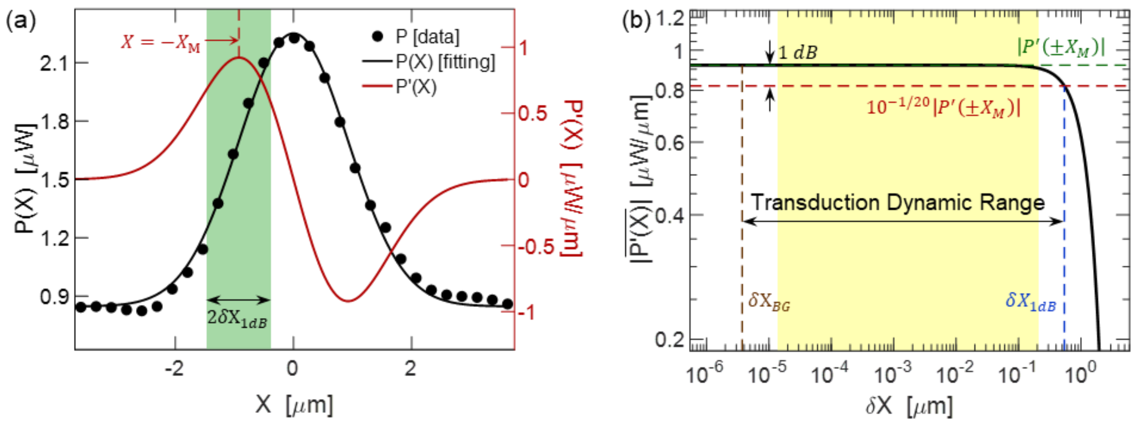

Figure S4. Transduction Dynamic Range. (a) Collected power profile from Figure S2b (dots) fitted to a Gaussian curve (black line) whose derivative (red solid line) reveals the optimum transduction positions $\pm X_M$, with $X_M = 0.924\mu m$ and $|P'(\pm X_M)| = 0.92\ \mu W/\mu m$. The green area indicates the extension of the linear transduction range, according to the 1 dB compression criterion followed here. **(b)** Average transduction sensitivity as a function of the peak vibration amplitude, calculated according to (S42), from which a value $DR(\text{transduction}) = 103\ dB$ is obtained for a resolution bandwidth $\Delta f = 1.098\ Hz$. The yellow area indicates the extension of the intrinsic mechanical dynamic range of the nanowire.

whose absolute value shows two symmetric maxima at points $X = \pm X_M$, with $X_M = B$. These symmetric maxima correspond to the optimum X positions regarding transduction sensitivity discussed in section 3.2 (local maxima in Figure S2d). The collected power profile, the Gaussian fitting and its derivative are shown in Figure S4a. The fitting provides an optimum transduction position $X_M = 0.924\ \mu m$ with a power gradient of $|P'(\pm X_M)| = 0.92\ \mu W/\mu m$. This value of the power gradient can be taken as an upper limit for an estimation of the transduction sensitivity, given that 1) it refers to the projection of the nanowire vibration along the X direction, which is lower than the actual vibration amplitude and 2) it corresponds to a point along the nanowire in the Z direction where $P'(X)$ is maximum, which is not necessarily at the tip, where the vibration amplitude is maximum.

Now we want to determine how the transduction sensitivity degrades as the amplitude of vibration increases. As a first order approximation, we characterize this degradation by computing the average sensitivity $\left|\overline{P'(X)}\right|$ along an $|X|$ interval ranging from $X_M - \delta X$ to $X_M + \delta X$, where δX is the peak amplitude of vibration:

$$\left|\overline{P'(X)}\right| = \left|\frac{\int_{X_M-\delta X}^{X_M+\delta X} P'(X)dX}{\int_{X_M-\delta X}^{X_M+\delta X} dX}\right| = \frac{1}{2\delta X}\left|[P(X)]_{X_M-\delta X}^{X_M+\delta X}\right| \qquad \text{(S41)}$$

Thus, after evaluating $P(X)$ at the integration boundaries, we obtain the average transduction sensitivity at the optimum transduction points $\pm X_M$ as a function of vibration amplitude δX:

$$\left|\overline{P'(X)}\right| = \frac{A}{2\delta X} e^{-\frac{(X_M-\delta X)^2}{2X_M^2}} \left[1 - e^{-\frac{2\delta X}{X_M}}\right] \tag{S42}$$

Now, in consistency with the definition used for the dynamic range of the nanowires, we define the upper limit for the transduction linear range as the 1 dB compression point for the transduction sensitivity. Therefore, the transduction 1 dB compression amplitude δX_{1dB} is defined as the peak amplitude for which $\left|\overline{P'(X)}\right|$ decays 1 dB with respect to the maximum value $|P'(\pm X_M)|$:

$$\frac{\frac{A}{2\delta X_{1dB}} e^{-\frac{(X_M-\delta X_{1dB})^2}{2X_M^2}} \left[1 - e^{-\frac{2\delta X_{1dB}}{X_M}}\right]}{\frac{A}{B} e^{-1/2}} = 10^{1/20} \tag{S43}$$

By solving this equation numerically (see Figure S4b), we obtain a value $\delta X_{1dB} = 541$ nm for the onset of transduction nonlinearity. It must be noted that this value corresponds actually to the projection of the vibration amplitude along the X direction and to a laser incidence point not at the nanowire tip, so that it represents a lower limit estimation of the actual vibration amplitude at the onset of transduction nonlinearity. From the analysis described in the main text for determining the dynamic range of the nanowires, we can obtain a value for the amplitude at the onset of mechanical nonlinearity a_{1dB} for this nanowire. For a proper comparison with the value obtained for the onset of transduction nonlinearity, we convert the measurement of a_{1dB} into length units by using $|P'(\pm X_M)| = 0.92\ \mu W/\mu m$ for the transduction sensitivity, which results in $a_{1dB} = 213$ nm. Thus, the amplitude at onset of mechanical nonlinearity is a factor 0.39 (-8.1 dB) lower than the amplitude at the onset of transduction nonlinearity, which validates our determination of the mechanical 1 dB compression amplitude.

Regarding the lower limit of the transduction linear range, the fact that the thermomechanical amplitude at the natural frequency is above the transduction detection limit is evidenced by Figure S3. Again, by assuming a transduction sensitivity given by $|P'(\pm X_M)| = 0.92\ \mu W/\mu m$, we estimate a detection limit of 3.56 pm/$\sqrt{\text{Hz}}$ (PSD peak amplitude), which for our measurement bandwidth ($\Delta f = 1.098$ Hz) corresponds to an amplitude of $\delta X_{BG} = 3.73$ pm. Applying the same conversion factor, the thermomechanical peak amplitude at the natural frequency is $a_{TH} = 13.9$ pm, which is a factor 3.7 (11.4 dB) larger than the amplitude detection limit.

Finally, we can define the transduction dynamic range as the ratio of the transduction 1 dB compression amplitude to the detection limit, expressed in dB:

$$DR(\text{transduction}) = 20\log_{10}\left(\frac{\delta X_{1dB}}{\delta X_{BG}}\right) \tag{S44}$$

from which for the case of nanowire #18 considered above we obtain a transduction DR of 103 dB, significantly larger than the mechanical DR of 84 dB measured for this nanowire. This observation and the fact that the mechanical DR limits are within the transduction DR boundaries make the detection scheme used in this work suitable for studying and exploiting the intrinsic mechanical DR of nanowires comparable to those characterized here.